© 2024 Hefei Institutes of Physical Science, Chinese Academy of Sciences and IOP Publishing Printed in China

Plasma Sci. Technol. **26** (2024) 064004 (9pp) https://doi.org/10.1088/2058-6272/ad1fd9

Preparation of palladium-based catalyst by plasma-assisted atomic layer deposition and its applications in CO_2 hydrogenation reduction

Shouxian TANG (唐守贤), **Di TIAN** (田地), **Zheng LI** (李筝), **Zhengduo WANG** (王正铎), **Bowen LIU** (刘博文), **Jiushan CHENG** (程久珊) **and Zhongwei LIU** (刘忠伟)*

Laboratory of Plasma Physics and Materials, Beijing Institute of Graphic Communication, Beijing 102600, People's Republic of China

*E-mail of corresponding author: liuzhongwei@bigc.edu.cn

Received 24 October 2023, revised 15 January 2024
Accepted for publication 17 January 2024
Published 9 May 2024

Abstract

Supported Pd catalyst is an important noble metal material in recent years due to its high catalytic performance in CO_2 hydrogenation. A fluidized-bed plasma assisted atomic layer deposition (FP-ALD) process is reported to fabricate Pd nanoparticle catalyst over γ-Al_2O_3 or Fe_2O_3/γ-Al_2O_3 support, using palladium hexafluoroacetylacetonate as the Pd precursor and H_2 plasma as counter-reactant. Scanning transmission electron microscopy exhibits that high-density Pd nanoparticles are uniformly dispersed over Fe_2O_3/γ-Al_2O_3 support with an average diameter of 4.4 nm. The deposited Pd-Fe_2O_3/γ-Al_2O_3 shows excellent catalytic performance for CO_2 hydrogenation in a dielectric barrier discharge reactor. Under a typical condition of H_2 to CO_2 ratio of 4 in the feed gas, the discharge power of 19.6 W, and gas hourly space velocity of 10000 h^{-1}, the conversion of CO_2 is as high as 16.3% with CH_3OH and CH_4 selectivities of 26.5% and 3.9%, respectively.

Supplementary material for this article is available online

Keywords: atomic layer deposition, CO_2 hydrogenation, palladium based catalyst

(Some figures may appear in colour only in the online journal)

1. Introduction

The increasing emission of carbon dioxide (CO_2) causes serious environmental problems such as climate change and global warming [1]. To limit its negative impact on our environment, several strategies have been investigated, including the storage and capture of CO_2, direct use of CO_2 for food packaging [2], and conversion of CO_2 into value-added products [3]. Among them, the reduction of CO_2 to CO, CH_4, and CH_3OH is considered to be a promising process since the afforded products are important chemical feedstocks for the synthetic fuels by the Fischer-Tropsch process and the synthesis of various chemicals [4]. However, carbon dioxide is a very thermodynamically stable molecule with a dissociation energy of 799 kJ mol^{-1}. To lower the activation energy barrier, considerable catalytic systems have been investigated for the reduction of CO_2 using precious metals [5–8], transition metal [9], and their compounds [10] as catalysts. Another effective pathway for CO_2 conversion is plasma-based technology [11]. Generally, the low-temperature plasma consists mainly of ground or excited atoms and molecules, positive and negative ions, and energetic electrons (1–10 eV) [12–15]. The high-energy electrons make

* Author to whom any correspondence should be addressed.

CO_2 molecules active and are regarded as initiators of highly reactive chemical mixtures. So, CO_2 can be converted into the desired products by adjusting the discharge parameters [16]. In addition, the introduction of a catalyst into the plasma-based CO_2 reduction can improve the conversion rate as well as improve the selectivity of the desired products [1]. In other words, the synergistic effects of plasma catalysis can be obtained [17].

Precious metal NPs have received increasing attention in the field of catalytic hydrogenation of CO_2 due to their excellent catalytic properties and excellent chemical stability. Palladium (Pd) is one of the most important noble metals. The traditional method for CO_2 reduction catalyst preparation is the wet chemical method [18–20], which implies that the porous support material is impregnated with an aqueous solution of the Pd precursor, or the Pd NPs are reduced in solution by a chemical-reducing agent [21]. It is well known that the catalytic performance of a catalyst depends largely on the size and shape of the metal particles and their distribution on the support; moreover, the interaction between the support and the metal affects the catalytic activity and selectivity [22]. However, wet chemical methods not only result in wastage of precursors but may suffer from poor control of the catalyst structure, leading to a wide distribution of particle sizes and non-uniform distribution of catalytically active sites on the carrier. This structural complexity hinders the improvement of catalytic activity and selectivity for the desired products of CO_2 reduction. Therefore, there is a need to develop a synthetic method to achieve precisely controlled catalyst synthesis. Over the past two decades, atomic layer deposition (ALD) has aroused great interest in the fabrication of precisely controlled heterogeneous catalysts [23]. In a typical ALD process, two precursors were alternatively introduced into the deposition chamber separating with the inert gas. Due to the self-limiting behavior of the ALD surface reactions, the uniform deposition of the target material can be achieved on flat substrates or complex three-dimensional structures with high surface area or high aspect ratio trenches. Various single atoms, the sub-nanometer cluster (less than 20 atoms), or nanoparticles have been fabricated on different porous supports by varying the number of ALD cycles and the deposition temperature [24]. Pd(II) hexafluoroacetylacetonate [$Pd(hfac)_2$] has been shown to be a good candidate for Pd ALD because of its high vapor pressure and relatively high thermal decomposition temperature up to 230 °C on the oxide surface [25]. Liang *et al* used palladium hexafluoroacetylacetonate $Pd(hfac)_2$ and formalin as reactants to deposit Pd nanoparticles on Al_2O_3 by ALD technique at 200 °C [21]. It was found that the amount of Pd on Al_2O_3 support and the size of the Pd nanoparticles were controlled by the number of ALD cycles and the $Pd(hfac)_2$ pulse time. Mackus *et al* investigated how to precisely control the size of the nanoparticles by ALD in the synthesis of nanoparticles of palladium and platinum [26]. The results of TEM analysis confirmed that the size of the synthesized Pd and Pt nanoparticles can be precisely controlled to the size range relevant to the catalytic application by controlling the number of cycles of ALD. On the other hand, the distribution of the particle size also depends on the experimental conditions. All these results suggest that the metal ALD nucleation mechanism is crucial for further improvement in the preparation of controllable nanoparticle size and uniform distribution of ALD on large specific surface area supports [27].

The current work aims to prepare Pd-Fe_2O_3 catalysts over γ-Al_2O_3 support, in which Fe_2O_3 was prepared by impregnation method using iron nitrate as the precursor, and Pd nanoparticles were deposited via a fluidized-bed plasma assisted atomic layer deposition (FP-ALD) using palladium hexafluoroacetylacetonate [$Pd(hfac)_2$] as the Pd precursor. H_2 plasma was employed as a reducing agent. Compared to fixed-bed atomic layer deposition, FP-ALD is capable of good mixing, large gas-solid contact area, obvious size reduction of agglomerates, and good particle distribution [28]. Therefore, the high coating efficiency of mass and heat transfer can be obtained by employing the fluidized-bed atomic layer deposition. Moreover, the combination of H_2 plasma with fluidized-bed ALD makes the Pd deposition performed at a relatively low temperature (80 °C), which also contributes to reducing Pd nanoparticle agglomeration. The γ-Al_2O_3 was chosen as the substrate because of its more robust CO_2 adsorption capacity and smaller dielectric constant, which is conducive to the generation of plasma and thus promotes the activation of CO_2 molecules [29–31].

2. Experiment

2.1. Catalyst synthesis

10wt% Fe_2O_3 supported on γ-Al_2O_3 powder was synthesized by wet impregnation with iron nitrate ($Fe(NO_3)_3{\cdot}9H_2O$) dissolved in water. After adding γ-Al_2O_3 to the iron nitrate solution, the mixture was continuously stirred at room temperature for 12 h. Finally, it was dried at 120 °C and calcined at 450 °C for 5 h. The resulting catalyst was labeled as $10Fe_2O_3/Al_2O_3$.

The deposition of Pd nanoparticles over Fe_2O_3/Al_2O_3 powders (40–60 meshes) was performed in a home-built vertical FP-ALD reactor, which had been described elsewhere [32], and only the main features were outlined here (figure S1). The deposition chamber consists of a fused silica tube (50 mm in height and 25 mm in outer diameter) with the middle enlarged to an outer diameter of 50 mm. An electric clamshell-type oven was used to heat the deposition chamber. A silica plate (1 mm thick) with 900 pores (200 μm in diameter) was fixed on the bottom part of the tube, on which 1 g $10Fe_2O_3/Al_2O_3$ powders were placed. The $Pd(hfac)_2$ precursor was placed in a stainless-steel bubbler, and it was heated to 50 °C to ensure that the precursor vapor pressure was high enough for Pd deposition. High-purity (99.999%) Ar gas with a flow rate of 50 standard cubic centimeters (sccm) was introduced into the bubbler to carry Pd precursor vapor to the deposition chamber. Ar gas was also used as the purge gas to remove unreacted Pd precursor and the volatile byproducts generated during the deposition.

High-purity H_2 (99.999%) was employed as the discharge gas to produce H_2 plasma with a flow rate of 50 sccm. The upward gas flows were obtained by introducing Ar and H_2 gas streams from the bottom of the FP-ALD reactor. To avoid γ-Al_2O_3 powders entering the pump line, the upper exit of FP-ALD reactor was wrapped by a Cu grid (75 μm pore size). Two copper coils with a distance of 60 mm covered the outside of the reactor tube's expansion region and served as the high-voltage electrode and the ground electrode, respectively. The high-voltage electrode was connected to a dielectric barrier discharge power source (HV Power Supply Source, CTP-2000, Nanjing Suman Plasma Technology Co. LTD) with a peak-to-peak voltage of up to 30 kV and a variable frequency of 10–30 kHz. Before deposition, we evacuated the deposition chamber down to about 5 Pa. A typical FP-ALD cycle for Pd deposition consists of the following sequence: 5 s Pd(hfac)$_2$ pulse, 10 s Ar purge pulse, 10 s H_2 plasma pulse, the second 10 s Ar purge pulse, and 30 W input discharge power (E_{in}) under a working pressure of 50 Pa. A 60-cycle deposition process was performed over γ-Al_2O_3 and Fe_2O_3/γ-Al_2O_3 supports, and the Pd loading amounts were all found to be ~2%. Based on the loading masses of metal, the afforded catalysts were labeled as 2Pd/Al_2O_3 and 2Pd-10Fe_2O_3/Al_2O_3, respectively.

2.2. Characterization

The Pd loading amounts of 2Pd/Al_2O_3 and 2Pd-10Fe_2O_3/Al_2O_3 were analyzed by inductively coupled plasma-atomic emission spectroscopy (ICP-OES) (Puyu, EXPEC 6000). The crystal structure of the deposited samples was measured by X-ray diffraction (XRD) (Rigaku, MiniFlex600) with Cu-K_α radiation. The 2θ detection range is 30°–80°, with a step of 0.02° and a scanning speed of 4° min^{-1}. The chemical composition and impurity of the grown Pd were determined by X-ray photoelectron spectroscopy (XPS) (Thermo, Escalab 250Xi) with a monochromatic Al-K_α source (1486.6 eV). The particle size distribution and elemental profiles of the deposited samples were determined by scanning transmission electron microscopy with energy dispersive X-ray spectroscopy (STEM-EDS) (FEI Talos F200S).

The reduction properties of the deposited catalysts were determined by the temperature-programmed reduction method. A ChemBET Pulsar TPR/TPD automatic chemisorption analyzer (Quantachrome) was used for the test.

2.3. Catalytic performance

The catalytic performance of 2Pd/Al_2O_3 and 2Pd-10Fe_2O_3/Al_2O_3 for CO_2 reduction was evaluated in a dielectric barrier discharge (DBD) reactor at atmospheric pressure, as shown in figure 1. The DBD reactor consists of a fused silica tube (inner diameter = 9 mm), a stainless steel rod (outside diameter = 3 mm) as a high voltage electrode placed along the axis of the outer tube, and a stainless steel mesh wrapped around the outer surface of the quartz tube as a ground electrode. The high-voltage electrode is connected to a DBD power supply source (HV Power Supply Source, CTP-2000, Nanjing Suman Plasma Technology Co. LTD), which is able to provide a bipolar sine wave output with a peak-to-peak voltage of 0–30 kV at an AC frequency of 27.7 kHz. The peak-to-peak voltage and the current applied to the DBD reactor were measured with a digital oscilloscope (Tektronix company, DPO4104) using a high-voltage probe (Tektronix, P6015A) and a current probe (Tektronix 6021AC). The input discharge power was calculated according to the Lissajous method. CO_2 and H_2 gas flows regulated by mass flow controllers were premixed and then delivered to the DBD reactor with a total flow rate of 100 sccm, corresponding to a gas hourly space velocity (GHSV) of 10000 h^{-1}. A small amount of quartz wool was placed underneath the catalyst (100 mg) to allow gas flow and hold the catalyst powders.

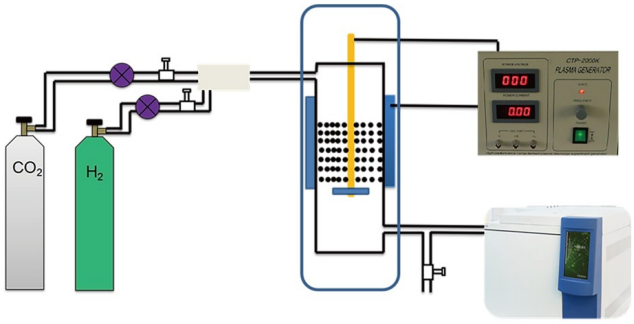

Figure 1. Schematic diagram of DBD experimental setup for CO_2 hydrogenation.

The amounts of gas products (CO and CH_4) and liquid phase products (CH_3OH) of CO_2 reduction were analyzed by an online gas chromatography (GC, INESA, GC126N) equipped with a thermal conductive detector (TCD) and a flame ionization detector (FID) using a TDX-D1 and HT-PLOT Q column. In this case, the liquid phase product is condensed and collected in a cold trap (0 °C) to be extracted and passed into the chromatography for detection. The conversion of CO_2 (X_{CO_2}) is defined as:

$$X_{CO_2}(\%) = \frac{\text{moles of } CO_2 \text{ converted}}{\text{moles of initial } CO_2} \times 100. \quad (1)$$

The selectivities (S) of the CO and CH_4 are defined as follows:

$$S_{CO}(\%) = \frac{\text{moles of CO produced}}{\text{moles of } CO_2 \text{ converted}} \times 100, \quad (2)$$

$$S_{CH_4}(\%) = \frac{\text{moles of } CH_4 \text{ produced}}{\text{moles of } CO_2 \text{ converted}} \times 100, \quad (3)$$

the selectivity of liquid CH_3OH was calculated by subtracting the selectivities of CO and CH_4 from 100%.

3. Results and discussion

3.1. Catalysts characterization

The crystal structures of the prepared 2Pd/Al_2O_3,

$10Fe_2O_3/Al_2O_3$, and $2Pd\text{-}10Fe_2O_3/Al_2O_3$ catalysts were analyzed by XRD. As shown in figure 2, the diffraction peaks centered at 45.8° and 66.7° can be assigned to γ-Al_2O_3 (PDF No. 29-0063); the other strong peaks marked at 35.6° and 54.1° can be ascribed to (100) and (116) planes of Fe_2O_3 (PDF No. 33-0664), indicating that iron oxide was successfully synthesized on γ-Al_2O_3 support. It is worth noting that Pd characteristic peaks at 40.1° for all samples are absent, since the Pd loading amount is as low as 2%. If Pd content rises to 10%, an obvious Pd diffraction peak (40.1°) can be observed, as shown in figure S2.

The chemical composition of the synthesized $2Pd/Al_2O_3$, $10Fe_2O_3/Al_2O_3$, and $2Pd\text{-}10Fe_2O_3/Al_2O_3$ catalysts was examined by XPS. A 2-keV Ar^+ beam bombards the deposited films for 40 s to remove the surface oxide and adventitious carbon before XPS measurements. Figure 3(a) shows the survey spectra of $2Pd\text{-}10Fe_2O_3/Al_2O_3$ sample. Photoelectron emission peaks display the presence of Pd, Fe, Al and O elements. Figures 3(b) and (c) represent the high-resolution XPS spectra for the core-level emission of Pd 3d and Fe 2p. As shown in figure 3(b), Pd 3d spectra depict pairs of spin-orbit split peaks corresponding to the high-energy Pd $3d_{3/2}$ band and low-energy Pd $3d_{5/2}$ band. For $2Pd/Al_2O_3$ sample, each peak can be deconvoluted into two sets of peaks of Pd^0 (335.2 and 340.4 eV) and Pd^{2+} (336.6 and 341.8 eV), and these values are consistent with the literature reports [33, 34]. During Pd precursor pulse, $Pd(hfac)_2$ would be chemisorbed on the substrate surface, and then reacted with H atoms contained within H_2 plasma, releasing some of the hfac ligand to convert Pd^{2+} metal ion into Pd^0. In the case of $2Pd\text{-}10Fe_2O_3/Al_2O_3$ sample, the values of Pd^{2+} binding energy were shifted by 0.5 eV to higher binding energy, which can be explained by the presence of a strong interaction between the Pd-Fe bimetals. Fe 2p spectra (figure 3(c)) display the $2p_{3/2}$–$2p_{1/2}$ double peaks at 711.2 eV and 725 eV for $10Fe_2O_3/Al_2O_3$ catalyst. When Pd was introduced into 10Fe_2O_3/Al_2O_3, a less pronounced blue shift can be found, implying again a stronger binding of electrons to Fe and thus a higher reduction.

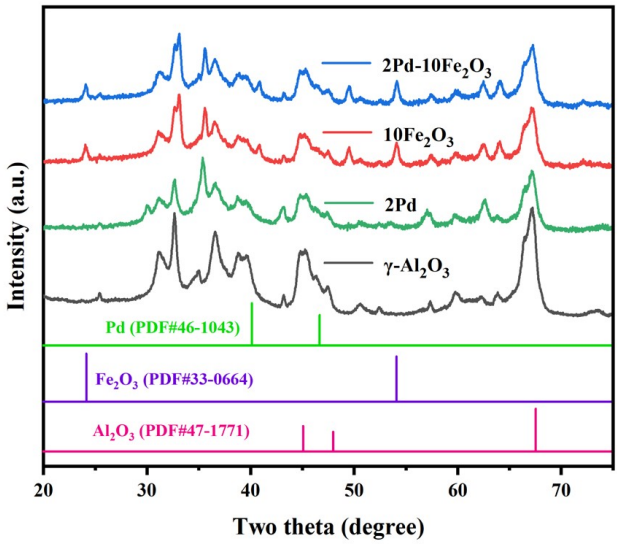

Figure 2. XRD patterns of $2Pd/Al_2O_3$, $10Fe_2O_3/Al_2O_3$, $2Pd\text{-}10Fe_2O_3/Al_2O_3$.

To further investigate the strong interaction between Pd and Fe_2O_3, the temperature-programmed reduction measurements for the prepared catalysts were performed on a Chem-BET Pulsar TPR/TPD automatic chemisorption analyzer. As shown in figure 4, for 2Pd sample, only one H_2 consumption peak centered at 90 °C was observed, and this number corresponds to Pd-O hydrogenation [35]. In regard to$10Fe_2O_3/Al_2O_3$ sample, three broad H_2 consumption peaks around 450 °C, 600 °C and 750 °C can be found, which are related to the reduction of Fe_2O_3 to Fe_3O_4, Fe_3O_4 to FeO and FeO to metallic Fe process [36, 37]. Regarding $2Pd\text{-}10Fe_2O_3/Al_2O_3$ sample, four clear H_2 reduction signals were identified: one located at 220 °C attributable to the reduction of Pd-O, and the others centered at 360 °C, 600 °C and 750 °C attributable to the reduction of Fe-O. Compared to $2Pd/Al_2O_3$ and $10Fe_2O_3/Al_2O_3$, the TPR temperature of Pd-O in $2Pd\text{-}10Fe_2O_3/Al_2O_3$ was shifted towards higher number (from 90 °C to 220 °C), and that of Fe-O was sharply decreased (from 450 °C to 350 °C), indicating a strong interaction between Pd and Fe_2O_3, which is consistent with the results of XPS analysis. Consequently, $2Pd\text{-}10Fe_2O_3/Al_2O_3$ exhibits an enhanced catalytic activity for CO_2 hydrogenation, as shown in catalytic performance section.

STEM-EDS was used to evaluate the $2Pd\text{-}10Fe_2O_3/Al_2O_3$ catalyst and the experimental results are shown in figure 5. For comparison, STEM-EDS images for γ-Al_2O_3 and $10Fe_2O_3/Al_2O_3$ samples are exhibited in figures S3 and S4. EDS images showed that high-density iron nanoparticles

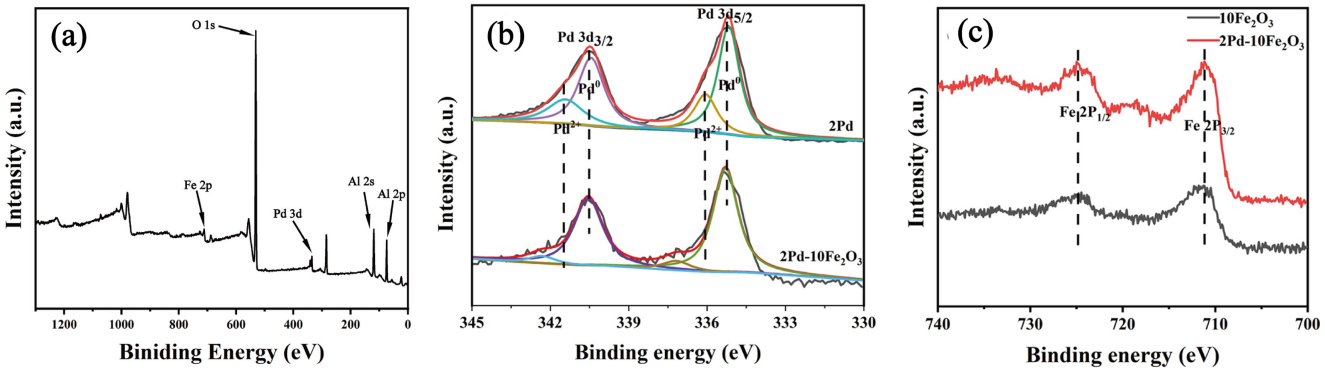

Figure 3. XPS of $2Pd/Al_2O_3$, $10Fe_2O_3/Al_2O_3$, $2Pd\text{-}10Fe_2O_3/Al_2O_3$. (a) Survey, (b) Pd 3d spectra, (c) Fe 2p spectra.

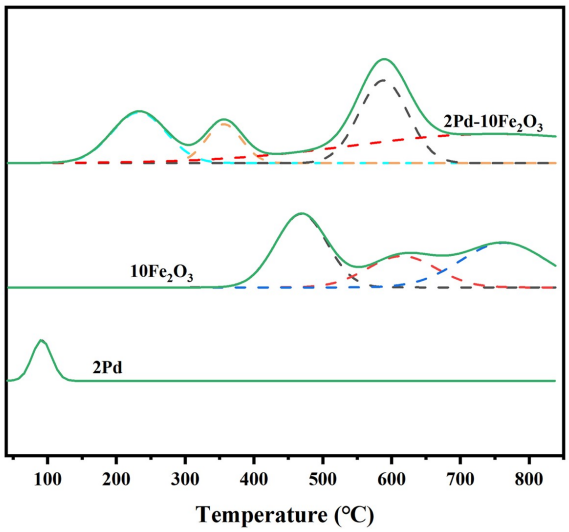

Figure 4. TPR diagram of $2Pd/Al_2O_3$, $10Fe_2O_3/Al_2O_3$, $2Pd\text{-}10Fe_2O_3/Al_2O_3$.

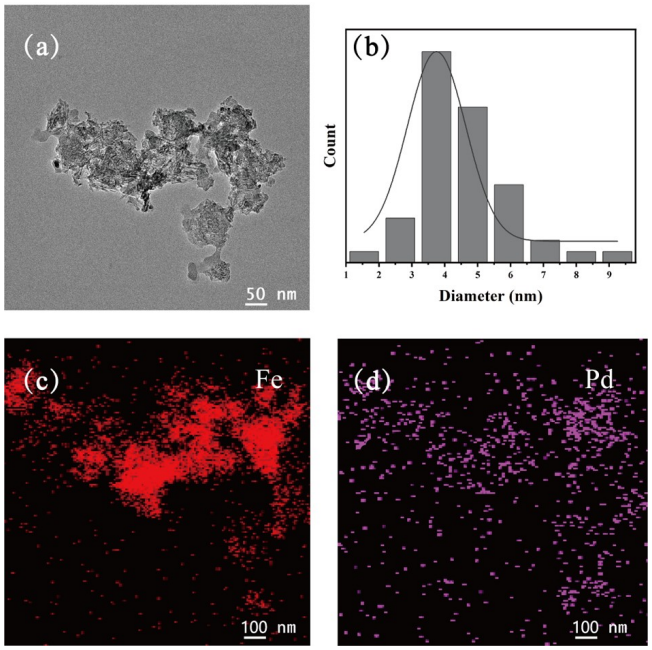

Figure 5. (a) STEM image of $2Pd\text{-}10Fe_2O_3/Al_2O_3$, (b) the particle size distribution diagram of $2Pd\text{-}10Fe_2O_3/Al_2O_3$, (c) distribution of Fe elements in $2Pd\text{-}10Fe_2O_3/Al_2O_3$ EDS images, (d) distributions of Pd and Fe elements in $2Pd\text{-}10Fe_2O_3/Al_2O_3$ EDS images.

were deposited over $\gamma\text{-}Al_2O_3$ support and distributed uniformly on the whole $\gamma\text{-}Al_2O_3$. Figure 5(b) shows that the high-density Pd nanoparticles were deposited on $10Fe_2O_3/Al_2O_3$ support. EDS mapping shown in figure 5(c) displays that Pd is uniformly dispersed on $10Fe_2O_3/Al_2O_3$ support. The average Pd particle size is about 4.4 nm obtained from TEM image shown in figure 5(b).

3.2. Catalytic performance

In the following part, the catalytic activity of $10Fe_2O_3/Al_2O_3$ and $2Pd\text{-}10Fe_2O_3/Al_2O_3$ for CO_2 hydrogenation was examined. Prior to catalytic performance measurements, the DBD discharge characteristics were evaluated. Figure 6(a) showed the waveforms of DBD discharge voltage and current without catalyst, where the peak-to-peak voltage and the frequency are 9.8 kV and 27.7 kHz, respectively. The numerous peaks in the current curve revealed the typical filamentary discharge characteristic. If the catalyst was introduced into the discharge region, the peak-to-peak voltage slightly rose to 10.8 kV, while the discharge frequency kept stable, as shown in figure 6(b). In a filled-bed DBD reactor, the discharge filaments can only be generated in the small gaps between the pellet-particle and pellet-quartz walls. As a result, the average electric field of the catalyst was enhanced [38]. The discharge power was calculated to be 20 W based on Lissajous plots in figure 6(c), and the presence of catalyst or not had a negligible effect on the input power.

Figure 7 shows the CO_2 conversion and the selectivity of CO, CH_4 and CH_3OH for catalyst samples of bare $\gamma\text{-}Al_2O_3$, $2Pd/Al_2O_3$, $10Fe_2O_3/Al_2O_3$ and $2Pd\text{-}10Fe_2O_3/Al_2O_3$ with H_2/CO_2 ratio of 4 at E_{in} = 19.6 W. As can be seen from figure 7, the addition of a catalyst to the CO_2 reduction reactor has more or less affected the conversion rate and product selectivity of CO_2. With plasma alone, the conversion of CO_2 is 6.7%. When $\gamma\text{-}Al_2O_3$, $2Pd/Al_2O_3$, $10Fe_2O_3/Al_2O_3$ were added to the reactor, the conversions of CO_2 slightly increased (7.6%–10.2%). In comparison, the conversion of CO_2 for $2Pd\text{-}10Fe_2O_3/Al_2O_3$ catalyst was as high as 16.3%. The possible reason for conversion improvement can be ascribed to the physical and chemical effects. As Neyts *et al* pointed out [15], the introduction of catalysts into the plasma is able to enhance the electric field, generate the micro-discharge inside the catalyst pores and change the discharge

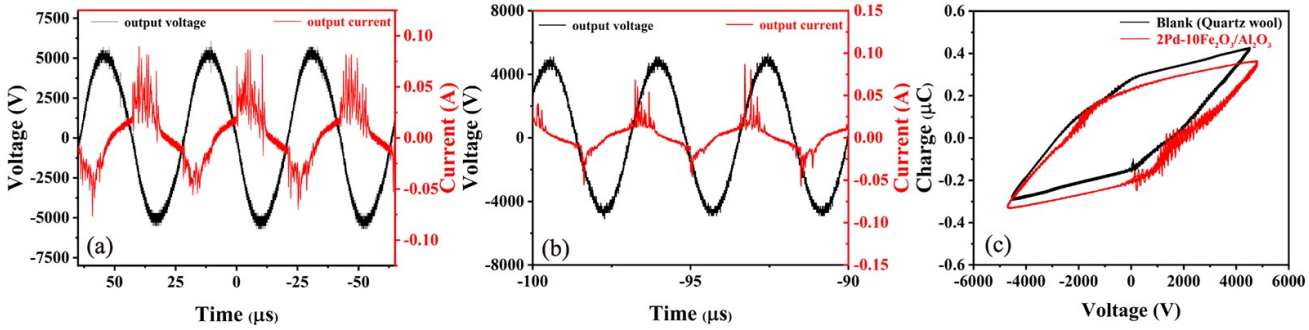

Figure 6. (a) Current-voltage waveform for unfilled catalyst, (b) current-voltage waveform for $2Pd\text{-}10Fe_2O_3/Al_2O_3$ filled catalyst, and (c) corresponding discharge voltage-charge Lissajous plot.

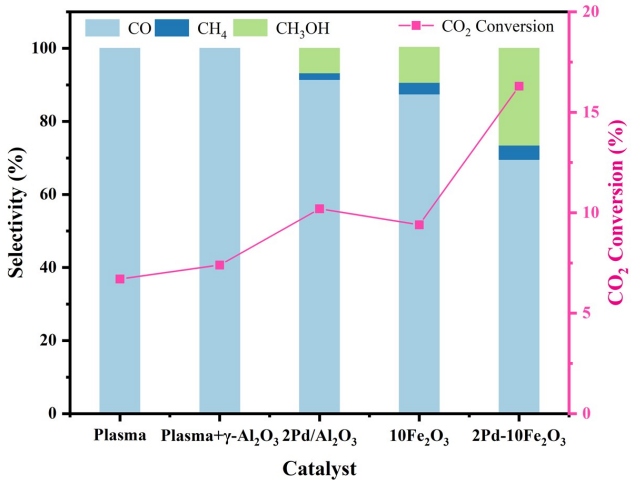

Figure 7. Effect of different catalysts on the performance of CO_2 hydrogenation reaction.

type (physical effect); on the other hand, the addition of catalysts can lower the activation barrier for specific reaction, increase the adsorption probability of species over the catalyst and alter the reaction pathway (chemical effect). For CO_2 hydrogenation over 2Pd-10Fe_2O_3/Al_2O_3 catalyst, another important effect should be considered besides the physical and chemical effects mentioned above, that is, the synergistic effect between Pd and Fe components. In general, the d-band centers of bimetallic catalysts are closer to the Fermi energy level and interact more strongly. The synergistic effect may be the mutual charge transfer between the d-band centers of transition metals, which are confirmed by XPS and TPR measurements. As a result, the mutual charge transfer leads to the enhanced adsorption properties of CO_2 and H^*, promoting the conversion of CO_2 reduction effect [39].

The dependence of the product selectivity on different catalyst samples is further shown in figure 7. When plasma alone or γ-Al_2O_3 was used, only CO was obtained, suggesting that Pd and Fe_2O_3 are required to convert CO_2 into the products of CH_3OH and CH_4. In contrast, the bimetallic 2Pd-10Fe_2O_3/Al_2O_3 catalyst could afford a high selectivity of 26.5% for CH_3OH and a comparable selectivity of 3.9% for CH_4. These results have clearly demonstrated the synergy of Pd, Fe_2O_3 and plasma for converting CO_2 into CH_4 and CH_3OH.

Figure 8 displays CO_2 conversion and product selectivity for 2Pd-10Fe_2O_3/Al_2O_3 catalyst as functions of H_2 to CO_2 ratio. With the total gas flow rate of 100 sccm and the input energy of 19.6 W, the conversion of CO_2 increased slowly from 8.9% to 10.3%, as H_2 to CO_2 ratio was raised from 1 to 4. Then, X_{CO_2} sharply rose to 16.3% at H_2/CO_2 ratio of 4, as shown in figure 8(a). The influence of H_2/CO_2 ratio on the product selectivity has been examined (figure 8(b)). With an increasing H_2/CO_2 ratio from 1 to 4, S_{CO} decreased linearly from 92.63% to 73.5%, and S_{CH_3OH} increased monotonously from 6.3% to 26.5%. As Chen *et al* pointed out [40], higher initial H_2 content in the feeding gas leads to higher atomic H density, and higher kinetic electrons. As a result, ionization

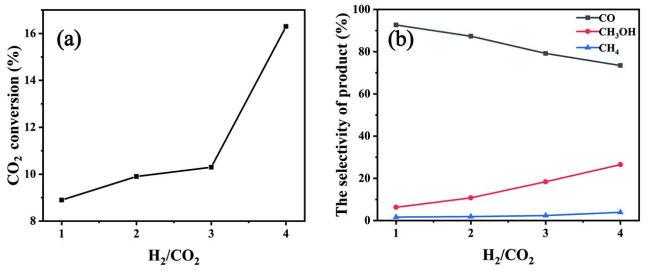

Figure 8. Effects of different H_2/CO_2 molar ratios on methanol synthesis by CO_2 hydrogenation.

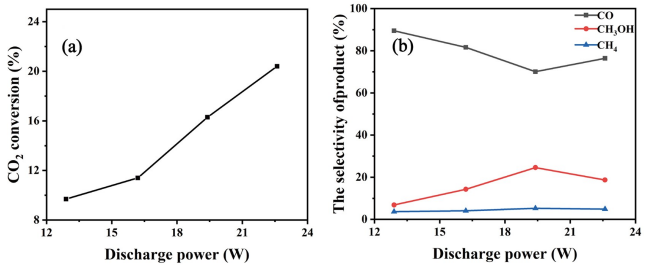

Figure 9. Effects of different discharge powers on the synthesis of methanol by hydrogenation of carbon dioxide.

rates can be expected in favor of higher methane and methanol number densities.

The effect of the input discharge power (E_{in}) on the conversion of CO_2 for 2Pd-10Fe_2O_3/Al_2O_3 catalyst was further investigated (figure 9). X_{CO_2} increases monotonously as the input discharge power increases, indicating the essential role of plasma in CO_2 reduction. In fact, DBD plasma contains numerous randomly distributed micro-discharge pulses (luminous filaments). The breakdown voltage to generate filaments is considered to be constant for a certain electrode spacing and a certain gas pressure and composition, that is, the breakdown voltage may not be changed with the applied peak-to-peak voltage. However, higher input discharge power (obtained by increasing the applied voltage) is able to produce more electrons with sufficient energy. These electrons generate more active intermediates, which is beneficial to the conversion of CO_2.

Figure 9(b) shows the selectivities of CH_4, CO and CH_3O H as functions of the input discharge power. S_{CH_4} keeps almost constant with increasing E_{in}. However, S_{CO} and S_{CH_3OH} display a minimum number and a maximum one at E_{in} = 19.6 W. From a thermodynamic point of view, the conversion of CO_2 into CH_3OH is an exothermic process. So, higher input discharge power, resulting in a higher discharge temperature, has a negative effect on S_{CH_3OH}. On the other hand, the positive effect of input discharge power for CH_3OH production very likely comes from the reactions of electron-based CO_2 reduction. The competition of the above negative and positive influence leads to a maximum value of S_{CH_3OH} at input discharge power of 19.6 W.

Under the above experimental conditions, we tested the stability of the 2Pd-10Fe_2O_3/Al_2O_3 catalyst with the highest CO_2 conversion, as shown in figure 10. The 2Pd-10Fe_2O_3/Al_2O_3 catalyst was placed into the CO_2 hydrogenation reactor for 30 h without stopping, and we collected data

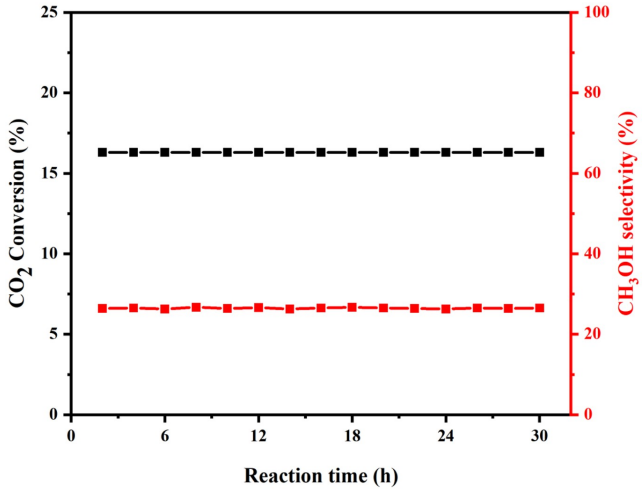

Figure 10. Stability test chart of 2Pd-10Fe_2O_3/Al_2O_3 catalyst.

at 2 h intervals. As can be seen from figure 10, the catalytic performance of the catalyst always remained the same, which indicates that no carbon accumulation occurred on the surface of the 2Pd-10Fe_2O_3/Al_2O_3 catalyst under the plasma action. Therefore, it could allow the catalyst to maintain good activity and stability all the time.

3.3. The reaction pathway for catalysts

The exploration of plasma-catalyst synergism is a very complex process, including the gas-phase reactions and the interacting surface processes. The main gas-phase reactions concerning plasma-based CO_2 hydrogenation are summarized in table 1. The interacting surface processes are related to direct adsorption, Eley-Rideal (E-R) reaction between gas-phase species and surface-adsorbed species, Langmuir-Hinshelwood (L-H) reactions, as well as dissociative adsorption and desorption [41].

In terms of gas-phase reactions, high-energy electron collisions lead to the dissociation of CO_2 and H_2, in which the electron collision dissociation reaction of H_2 (R1: $e + H_2 \Rightarrow e + 2H$) is the most efficient pathway for the production of H atoms. The electron collision ionization reaction of H (R4: $e + H \Rightarrow 2e + H^+$) is the most efficient pathway for H loss of reaction, followed by R11 ($H + H + M \Rightarrow H_2 + M$), R12 ($H + O + M \Rightarrow OH + M$) and R13 ($O^- + H \Rightarrow OH + e$), where M is a third body to carry off the excess energy in the reaction process. CO is produced from the dissociation of CO_2 (R2: $e + CO_2 \Rightarrow e + CO + O$), and O_2 is produced directly via electron collisional ionization (R3: $e + CO_2 \Rightarrow 2e + O_2 + C^+$). The electron collisional ionization reactions of CO (R5: $e + CO \Rightarrow 2e + CO^+$, R6: $e + CO \Rightarrow 2e + C^+ + O$, and R7: $e + CO \Rightarrow 2e + C + O^+$) are the three main destructive reactions of CO. In addition, R14 ($H + CO + M \Rightarrow CHO + M$) is also considered one of main CO loss reactions. The product of CHO is considered to be an important intermediate in the synthesis of methanol [40]. However, the contribution of the generation reaction associated with CH_3OH is reported in the literature to be about 10^{-25} mol/m, which is much lower than that of the reactions associated with H and CO (10^{-10} mol/m), so it is necessary to consider interacting surface processes to transfer a large amount of carbon and hydrogen into methanol.

Based on the previous reports [42, 43], we make a reasonable speculation on the reaction mechanism for the preparation of CH_3OH by DBD CO_2 hydrogenation over 2Pd-10Fe_2O_3/Al_2O_3 catalyst. The main reaction pathways for CH_3OH production are as follows:

(1) C atoms dissociated from the CO_2 molecule combine with H_2 to form hydrocarbons (CH, CH_2), and then these hydrocarbons react with CO_2 to produce oxygenated compounds (CHO, CH_2O). Finally, the sequential H addition reaction in CHO produces methanol.

(2) The C and O atoms dissociated from CO_2 are successively hydrogenated to produce CH_3 and OH, respectively, and finally, the reaction of CH_3 and OH^- or the hydrogenation of CH_2OH produces methanol.

As stated in the above study, it is clear that the first one is the main pathway for CH_3OH production. The postulated solid-phase reaction mechanism is shown in figure 11.

Table 11. Chemical reactions and active species in DBD-CO_2 hydrogenation [44]

Index	Reaction formula	Rate constant	Type	Species	Density (m^{-3})
R1	$e + H_2 \Rightarrow e + 2H$	–	Ground State Species	CO	10^{20}
R2	$e + CO_2 \Rightarrow e + CO + O$	–		CO^+/H_3O^+	10^{18}
R3	$e + CO_2 \Rightarrow 2e + O_2 + C^+$	–		$H_2O^+/O^-/H^-$	10^{17}
R4	$e + H \Rightarrow 2e + H^+$	–	Radicals	H/O	10^{22}
R5	$e + CO \Rightarrow 2e + CO^+$	–			
R6	$e + CO \Rightarrow 2e + C^+ + O$	–			
R7	$e + CO \Rightarrow 2e + C + O^+$	–			
R8	$H_2 + OH \Rightarrow H + H_2O$	1.01×10^{-15}			
R9	$O^+ + H_2 \Rightarrow H_2O^+ + H$	1.7×10^{-15}			
R10	$H_2O + H_2 \Rightarrow H_3O^+ + CO_2$	6.4×10^{-16}			
R11	$H + H + M \Rightarrow H_2 + M$	6×10^{-45}			
R12	$H + O + M \Rightarrow OH + M$	4.33×10^{-44}			
R13	$O^- + H \Rightarrow OH + e$	5×10^{-16}			
R14	$H + CO + M \Rightarrow CHO + M$	1.54×10^{-46}			

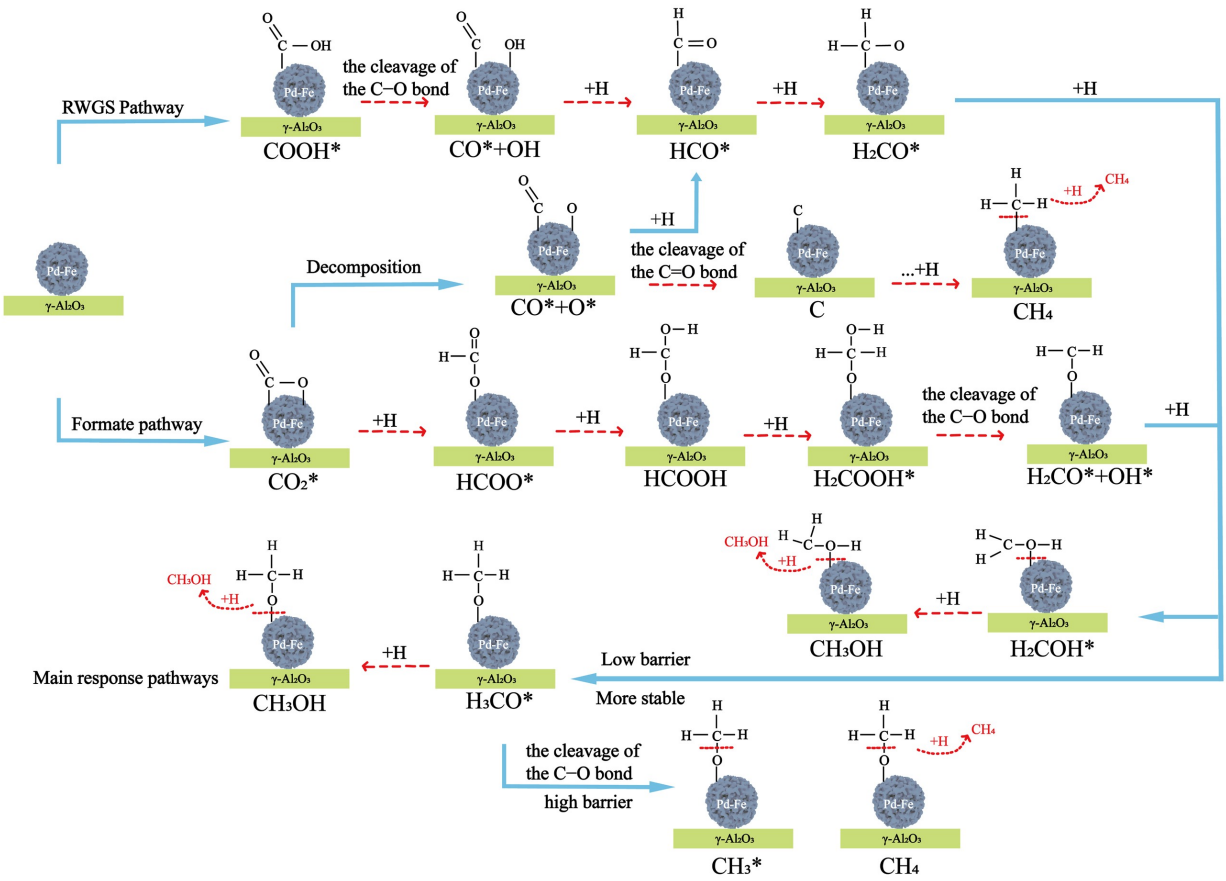

Figure 11. Possible main reaction pathways for plasma-induced hydrogenation of CO_2 in the solid phase.

4. Conclusions

In conclusion, Pd based nanoparticle catalyst has been successfully deposited by a fluidized-bed plasma assisted atomic layer deposition technique. With a FP-ALD sequence of 5 s Pd(hfac)$_2$ pulse, 10 s Ar purge pulse, 10 s H_2 plasma pulse, the second 10 s Ar purge pulse, 30 W input discharge power, and 80 °C deposition temperature, highly-density Pd nanoparticles with the average diameter of 4.4 nm, were uniformly distributed over Fe_2O_3/Al_2O_3 support, according to STEM-EDS measurements. H_2-TPR results suggest a strong interaction between Pd and Fe_2O_3. With the loadings of 2% and 10% for Pd and Fe_2O_3, respectively, the deposited 2Pd-10Fe_2O_3/Al_2O_3 shows excellent catalytic activity for CO_2 hydrogenation in DBD plasmas. Under a typical condition of H_2/CO_2 = 4, E_{in} = 19.6 W, and GHSV = 10000 h^{-1}, the conversion of CO_2 is as high as 16.3% with CH_3OH and CH_4 selectivities of 26.5% and 3.9%, respectively. This result has clearly demonstrated the synergistic effect of Pd, Fe_2O_3 and plasma for conversion of CO_2.

Acknowledgments

This work was financially supported by National Natural Science Foundation of China (Nos. 12075032 and 12105021), Beijing Municipal Natural Science Foundation (Nos. 8222055 and 2232061), Yunnan Police College Project (No. YJKF002), and Beijing Institute of Graphic Communication Project (No. Ec202207).

References

[1] Li J *et al* 2019 *Nanomaterials* **9** 1428
[2] Leonzio G, Fennell P S and Shah N 2022 *Appl. Sci.* **12** 8321
[3] Kumaravel V, Bartlett J and Pillai S C 2020 *ACS Energy Lett.* **5** 486
[4] Sempuga B C and Yao Y 2017 *J. CO_2 Util.* **20** 34
[5] Wang L *et al* 2018 *ACS Catal.* **8** 90
[6] Jwa E *et al* 2013 *Fuel Process. Technol.* **108** 89
[7] Nizio M *et al* 2016 *Int. J. Hydrogen Energy* **41** 11584
[8] Mikhail M *et al* 2020 *Catal. Sci. Technol.* **10** 4532
[9] Grice K A 2017 *Coord. Chem. Rev.* **336** 78
[10] Zeng Y X and Tu X 2016 *IEEE Trans. Plasma Sci.* **44** 405
[11] Wanten B *et al* 2023 *J. Energy Chem.* **86** 180
[12] Yu F and Di L B 2020 *Nanomaterials* **10** 333
[13] Li Z *et al* 2018 *Acta Phys. Sin.* **67** 215202
[14] Ashford B *et al* 2020 *Appl. Catal. B Environ.* **276** 119110
[15] Neyts E C *et al* 2015 *Chem. Rev.* **115** 13408
[16] Snoeckx R and Bogaerts A 2017 *Chem. Soc. Rev.* **46** 5805
[17] Chung W C and Chang M B 2016 *Renew. Sustain. Energy Rev.* **62** 13
[18] Wang J J *et al* 2021 *Green Chem.* **23** 1642
[19] Ahouari H *et al* 2013 *React. Kinet. Mech. Catal.* **110** 131
[20] Han A Z, Ding J and Zhong Q 2022 *Colloids Surf. A Physicochem. Eng. Asp.* **641** 128535

[21] Liang X H and Yaghobi N 2012 *J. Nanopart Res.* **14** 1
[22] Kwak J H, Kovarik L and Szanyi J 2013 *ACS Catal.* **3** 2449
[23] Lu J L, Elam J W and Stair P C 2016 *Surf. Sci. Rep.* **71** 410
[24] Ramesh R *et al* 2021 *Adv. Mater. Interfaces* **8** 2001508
[25] Senkevich J J *et al* 2002 *Chem. Vap. Deposition* **8** 189
[26] Mackus A J M *et al* 2016 *Nanotechnology* **27** 034001
[27] Di L B *et al* 2021 *J. Phys. D: Appl. Phys.* **54** 333001
[28] Peng Z B *et al* 2016 *Adv. Powder Technol.* **27** 2342
[29] Feliz M Q *et al* 2021 *J. Phys. D: Appl. Phys.* **54** 334003
[30] Zhu M *et al* 2022 *J. Phys. D: Appl. Phys.* **55** 225207
[31] Duan X F *et al* 2015 *AICHe J.* **61** 898
[32] Wang D Y *et al* 2022 *J. Vac. Sci. Technol. A* **40** 062404
[33] Brun N *et al* 2013 *New J. Chem.* **37** 157
[34] Tsang C H A *et al* 2014 *J. Mater. Chem. A* **2** 17986
[35] Wang W *et al* 2000 *Appl. Catal. B* **24** 219
[36] Xu X W *et al* 2012 *Renew. Energy* **41** 23
[37] Rapagnà S *et al* 2011 *Catal. Today* **176** 163
[38] Wang W Z, Butterworth T and Bogaerts A 2021 *J. Phys. D: Appl. Phys.* **54** 214004
[39] Nie X W *et al* 2019 *J. CO_2 Util.* **29** 179
[40] Chen Y L *et al* 2022 *Jpn. J. Appl. Phys.* **61** 086001
[41] Du J *et al* 2022 *Plasma Process. Polym.* **19** 2100111
[42] Zhang Z Y *et al* 2023 *Carbon Lett.* **33** 973
[43] Michiels R, Engelmann Y and Bogaerts A 2020 *J. Phys. Chem. C* **124** 25859
[44] Liao Y K *et al* 2020 *J. Appl. Phys.* **128** 233303